Supplementary Material for

Topological Weyl Altermagnetism in CrSb

Cong Li[1,*,♯], Mengli Hu[2,*], Zhilin Li[3,*], Yang Wang[1], Wanyu Chen[1], Balasubramanian Thiagarajan[4], Mats Leandersson[4], Craig Polley[4], Timur Kim[5], Hui Liu[6,♯], Cosma Fulga[2,7], Maia G. Vergniory[8,9], Oleg Janson[2], Oscar Tjernberg[1,♯], Jeroen van den Brink[2,7,♯]

[1]*Department of Applied Physics, KTH Royal Institute of Technology, Stockholm 11419, Sweden*

[2]*Leibniz Institute for Solid State and Materials Research, IFW Dresden, Helmholtzstraße 20, 01069 Dresden, Germany*

[3]*Beijing National Laboratory for Condensed Matter Physics, Institute of Physics, Chinese Academy of Sciences, Beijing 100190, China*

[4]*MAX IV Laboratory, Lund University, 22100 Lund, Sweden*

[5]*Diamond Light Source, Harwell Campus, Didcot, OX11 0DE, United Kingdom*

[6]*Department of Physics, Stockholm University, AlbaNova University Center, 10691 Stockholm, Sweden*

[7]*Würzburg-Dresden Cluster of Excellence Ct.qmat, Technische Universitat Dresden, 01062, Dresden, Germany*

[8]*Max Planck Institute for Chemical Physics of Solids, 01187 Dresden, Germany*

[9]*Donostia International Physics Center, 20018 Donostia–San Sebastian, Spain*

[*]*These authors contributed equally to the present work.*

[♯]*Corresponding authors: conli@kth.se, hui.liu@fysik.su.se, oscar@kth.se, j.van.den.brink@ifw-dresden.de*

CONTENTS

Appendix A: Projected Wannier function

To study the topological properties of CrSb, we projected the VASP-calculated bands onto a Wannier basis using the maximally-localized Wannier functions formalism implemented in Wannier90. Fig. S1 shows that the Fourier-transformed Wannier Hamiltonian agrees very well with the DFT band structure. For further analysis, we additionally symmetrized the resulting hopping parameters such that they respect all symmetries of the magnetic space group $P6'_3/m'm'c$ (No. 194.268). We note that this symmetrization does not give rise to any discernible changes in the spectrum. All further discussions of the topology of CrSb are based on results obtained for this symmetrized Hamiltonian.

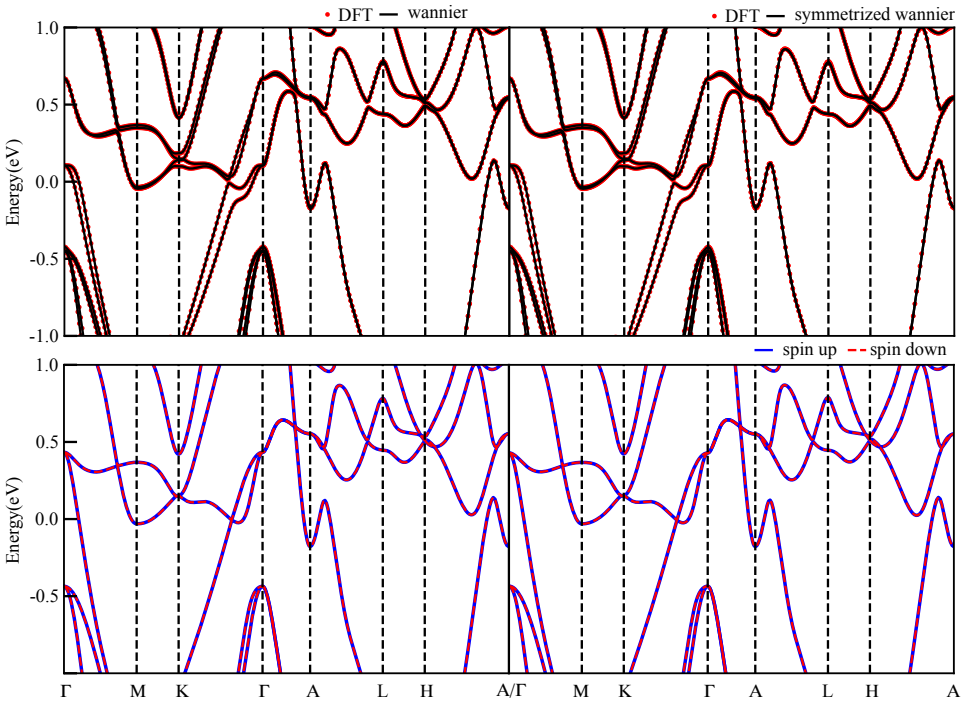

FIG. S1. **Wannier function projection comparison with DFT calculation** Upper panel: Band structure calculated by DFT labelled by red solid dots. Fitted Wannier functions and the symmetrized Wannier functions are presented on the left and right panels denoted by black solid lines, respectively. Lower panel: Band structure calculated by DFT without SOC. The left panel presents the band structure calculated based on symmetrized Wannier functions, and the right panel is the DFT calculation results. The calculated bands are along $\Gamma - M - K - \Gamma - A - L - H - A$.

We also performed the DFT calculation without SOC and did the corresponding Wannier

projection. As shown in the lower panel in Fig. S1, the symmetrized Wannier Hamiltonian also shows good consistency with the DFT results. To arrive at a symmetrized Hamiltonian, we averaged all symmetrically equivalent hopping parameters as explained in Ref. 1.

Appendix B: WPs locations

In our full relativistic calculations, i.e. with the spin-orbit coupling included, we have searched the Weyl points (WPs) spanning from the energy range of 1 eV around the Fermi level. In this way, we found 13 groups of WPs, for which we evaluated the corresponding spin expectation values. The respective spin operator in orbital and spin basis reads: $\sigma_z = I_N \bigotimes \sigma_z$, where N is the number of total number of basis divided by 2. The total spin expectation values for WPs take the form: $\langle S_z \rangle = \sum_i^2 \langle \phi_i | \hat{\sigma_z} | \phi_i \rangle /2$. We identify the type of WPs as same-spin when $| \langle S_z \rangle | > 0.9$ and opposite-spin when $| \langle S_z \rangle | \leq 0.2$. In this way, we classify them according to their spin values in the fully spin polarized (without SOC) limit: 1) opposite-spin WPs enforced by spin space group symmetry, 2) accidental opposite-spin WPs, and 3) same-spin WPs. For the first two types, WPs are labeled as Opposite-1 and Opposite-2 in the following tables. All 13 groups of WPs are sorted by their magnetic little co-groups.

Number of WPs	location (u,v,w)	Energy	Chirality	Type	$\langle S_z \rangle$
2.1	(-0.18323, 0.09917, -0.16014)	-0.62992	-1	Opposite-2	-0.174
3.1	(-0.26333, -0.07510, 0.21453)	0.12050	1	Same-spin	0.994
2.2	(0.36769, -0.52436, -0.16000)	0.30000	1	Opposite-2	0.007
2.3	(0.14573, -0.50290 , 0.37165)	0.33314	-1	Opposite-2	-0.020
2.4	(0.13637 , 0.35652, 0.39145)	0.34602	-1	Opposite-2	0.036
2.5	(-0.44259 , 0.13094, -0.08619)	0.32175	-1	Opposite-2	0.002
2.6	(-0.21457, 0.03116, -0.30092)	0.68000	1	Opposite-2	-0.038

TABLE I. WPs belonging to little co-group: 1. There are 24 symmetry connected WPs that share the same relation of location and chirality where WPs at (u,v,w),(v,-u-v,w),(-u-v,u,w),(-v,-u,-w),(-u,u+v,-w),(u+v,-v,-w),(u,v,-w),(v,-u-v,-w),(-u-v,u,-w),(-v,-u,w), (-u,u+v,w),(u+v,-v,w) share the chirality and at (-u,-v,-w),(-v,u+v,-w),(u+v,-u,-w),(v,u,w),(u,-u-v,w),(-u-v,v,w), (-u,-v,w),(-v,u+v,w),(u+v,-u,w),(v,u,-w),(u,-u-v,-w),(-u-v,v,-w) host opposite chirality.

Number of WPs	location	Energy	Chirality	Type	$\langle S_z \rangle$
3.2	(0.16200, 0.00000, -0.13500)	-0.35700	-1	Same-spin	0.981
3.3	(0.08556, 0.00000, 0.39873)	0.37304	1	Same-spin	-0.952
2.7	(-0.11043, 0.00000, -0.12601)	0.97800	1	Opposite-2	-0.017
1.1	(-0.37754, 0.01763, 0.00000)	0.33580	1	Opposite-1	0.000

TABLE II. WPs are belong to little co-group: $2'$. There are 12 symmetry connected WPs and for No. 3.2, No. 3.3, and No. 2.7, the symmetry connected WPs locations are (u,0,w),(0,-u,w),(-u,u,w),(0,-u,-w),(-u,u,-w),(u,0,-w),(-u,0,-w) have same chirality, and (0,u,-w), (u,-u,-w),(0,u,w),(u,-u,w),(-u,0,w) host opposite chirality to the first half WPs. No. 1.1 WPs are in the $k_z = 0$ plane and their Weyl pairs are (u,v,0),(v,-u-v,0),(-u-v,u,0),(-u,-v,0),(-v,u+v,0),(u+v,-u,0),(-v,-u,0),(-u,u+v,0),(u+v,-v,0),(v,u,0),(u,-u-v,0),(-u-v,v,0) where the first half share the same chirality and the remaining half is opposite.

Number of WPs	location	Energy	Chirality	Type	$\langle S_z \rangle$
1.2	(-0.17637 0.00000 0.00000)	0.30800	1	Opposite-1	-0.017
1.3	(0.00000 0.36304 0.00000)	0.32330	-1	Opposite-1	0.008

TABLE III. WPs belonging to little co-group: $2'2'2$. There are 6 symmetry connected WPs share the same relation of location and chirality where WPs are at (u,0,0),(-u,0,0),(0,u,0),(0,-u,0),(-u,u,0),(u,-u,0) and first half of them share the same chirality and the remaining half have opposite chirality of the first.

To visualize all the WPs, we divided these WPs into three categories and plotted their positions in the three-dimensional (3D) Brillouin zone in Fig. S2. Fig. S2a shows the 3D distribution of opposite spin WPs on the high symmetry line/plane in the 3D BZ (red dots representing points with chirality $\chi = +1$ and green dots representing $\chi =$ -1). Fig. S2b-S2c show the top view and side view of Fig. S2a which gives a more complete view of the distribution of WPs. The same group of WPs is connected with colored lines. Different colors represent the different energy positions of WPs. Fig. S2d-S2f and Fig. S2g-S2i show similar plots of the WPs as Fig. S2a-S2c but corresponding to opposite spin WPs for general momenta (Fig. S2d-S2f) and same spin WPs (Fig. S2g-S2i).

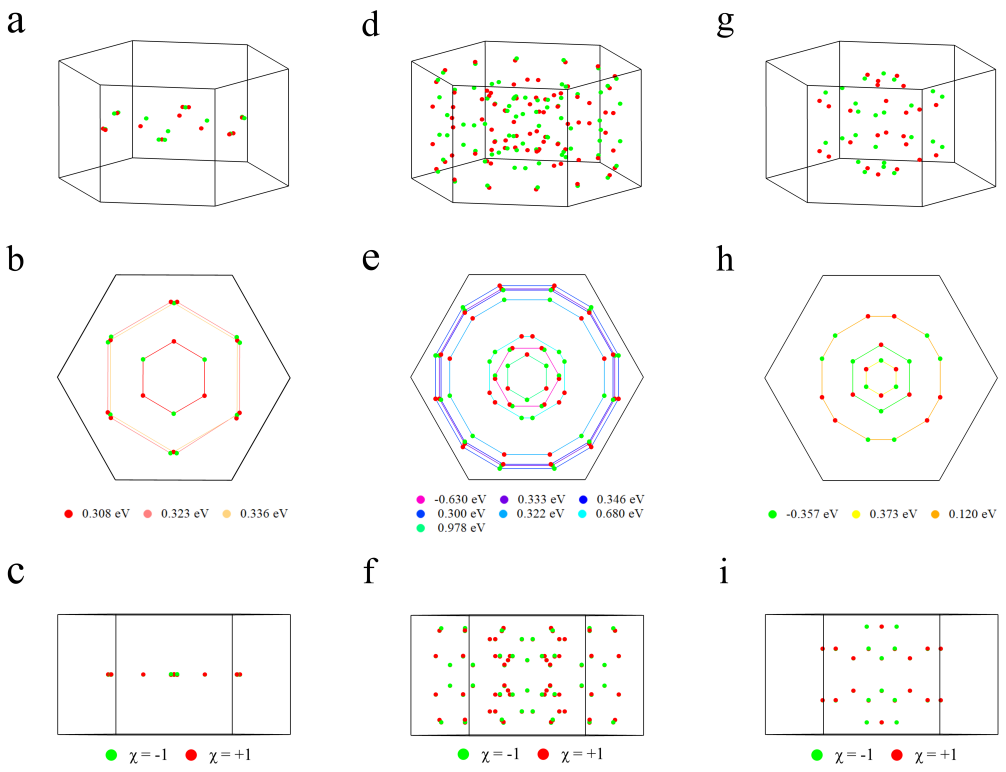

FIG. S2. **WPs of CrSb.** (a) The distribution of opposite spin WPs on the high symmetry line/plane in the 3D BZ, with the red dots representing points with chirality $\chi = +1$ and green dots representing χ = -1. (b-c) The top (b) and side (c) views of (a). The same group of WPs is connected with colored lines. Different colors represent the different energy positions of WPs. (d-f) The similar plot as (a-c) but corresponding to the opposite spin WPs on general momentum. (g-i) Similar plots as (d-f) but corresponding to the same spin WPs.

Appendix C: Calculation of CrSb surface states along high-symmetry lines

Fig. S3a-S3d show the spectral density from semi-infinite CrSb calculation. Using the iterative Green's function technique, the bulk (Fig. S3a-S3b), Sb (Fig. S3c), and Cr (Fig. S3d) terminated surface spectrum are obtained. To further analyze the surface states, Fig. S3e and Fig. S3f are the results with bulk weight subtracted.

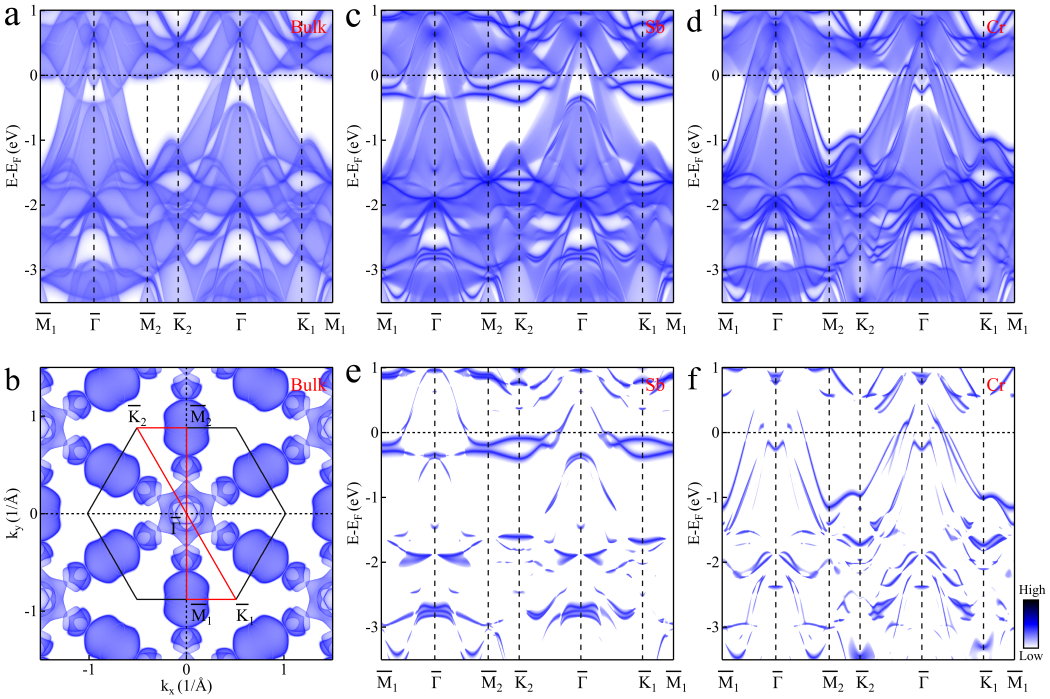

FIG. S3. **Surface state calculation along high symmetry lines** (a), (c), (d) are the calculated bulk and surface spectral densities along $\overline{\mathrm{M}}_1 - \overline{\Gamma} - \overline{\mathrm{M}}_2 - \overline{\mathrm{K}}_2 - \overline{\Gamma} - \overline{\mathrm{K}}_1 - \overline{\mathrm{M}}_1$. The high symmetry points are defined in (b). (b) is the bulk density of state in the BZ at the Fermi level. (e-f) are the surface spectral densities subtracted by bulk densities.

Appendix D: k_z dependent band structures of CrSb

Fig. S4 shows the in-plane band dispersion for various k_z, with the respective spin projections onto the x (Fig. S4a), y (Fig. S4b) and z (Fig. S4c) axes. As discussed in the main text, in the absence of SOC, doubly degenerate bands are confined to the four mirror planes. With SOC, degeneracies in the three vertical mirror planes are lifted, while those in the $k_z = 0$ plane remain. Nonsymmorphic symmetries [2] of the magnetic space group, e.g. a two-fold screw axis combined with time reversal, give rise to k_z-dependent degeneracy, which also happens in transition metal dichalcogenides [3, 4]. Along the $\widetilde{K} - \widetilde{\Gamma}$ high symmetry line, nonzero spin projection along the z direction is not allowed due to the mirror symmetry. Also WPs are not allowed on the mirror plane in CrSb. The band structure analysis for different k_z also reveals that SOC plays a role in breaking the nodal lines/surfaces in CrSb.

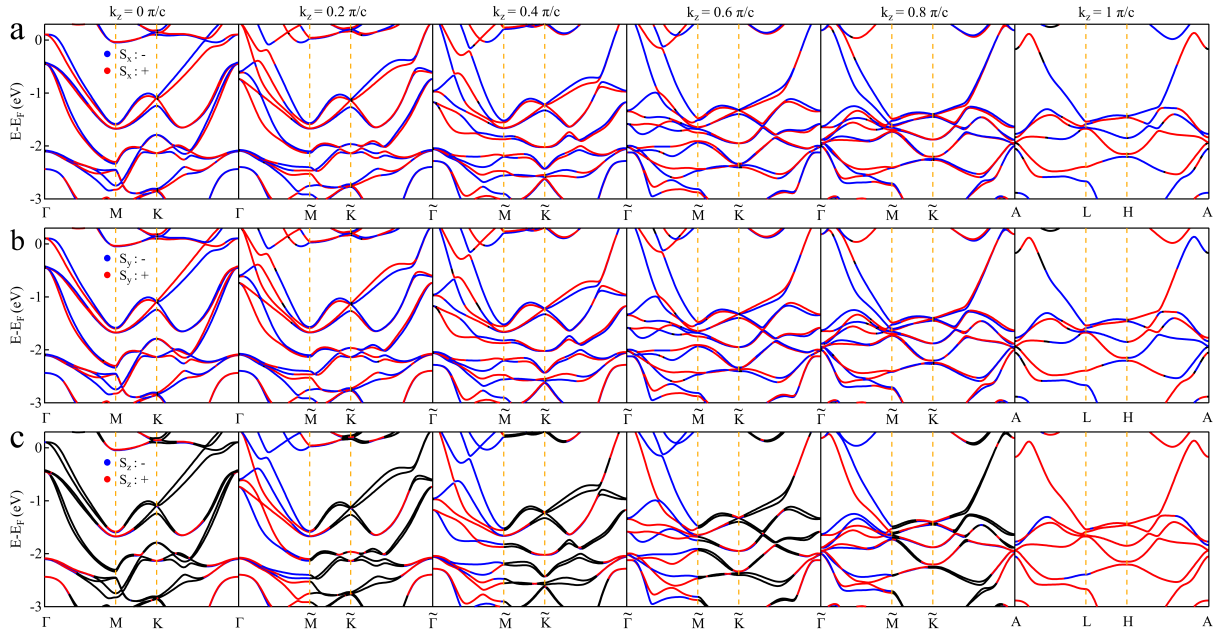

FIG. S4. **K_z dependent spin polarized band structures of CrSb.** (a-c) k_z dependent spin polarized band structures along $\widetilde{\Gamma} - \widetilde{\mathrm{M}} - \widetilde{\mathrm{K}} - \widetilde{\Gamma}$ with spin projected along the x (a), y (b) and z (c) directions. The red (blue) bands represent spin-up (spin-down) along the corresponding directions. Black bands represent spin degenerate bands.

Appendix E: Surface states of CrSb

Fig. S5 shows the calculated surface spectral density at the Fermi level of the Sb- (Fig. S5a and S5c) and Cr-terminated (Fig. S5b and S5d) surfaces. We use a logarithmic (linear) color scale in Fig. S5a and S5b (Fig. S5c and S5d). These figures are also shown in the main-text as Fig. 2a and 2b. To emphasize contributions of the surface states, bulk states have been subtracted following the equation: $\rho_s(\epsilon, \mathbf{k}) - \rho_{\mathbf{b}}(\epsilon, \mathbf{k})$ from Fig. S5c and S5d and the pure surface density results is shown in Fig. S5e and S5f. The SFAs are marked by orange arrows. For each projected WP on the (001) surface, there are two WPs with identical chirality at the same position in the 2D BZ, that give rise to two SFAs. SFAs labelled in Fig. S5e and S5f originate from WPs No. 3.2 and No. 3.3, whose positions along $\overline{\Gamma} - \overline{M}$ and denoted.

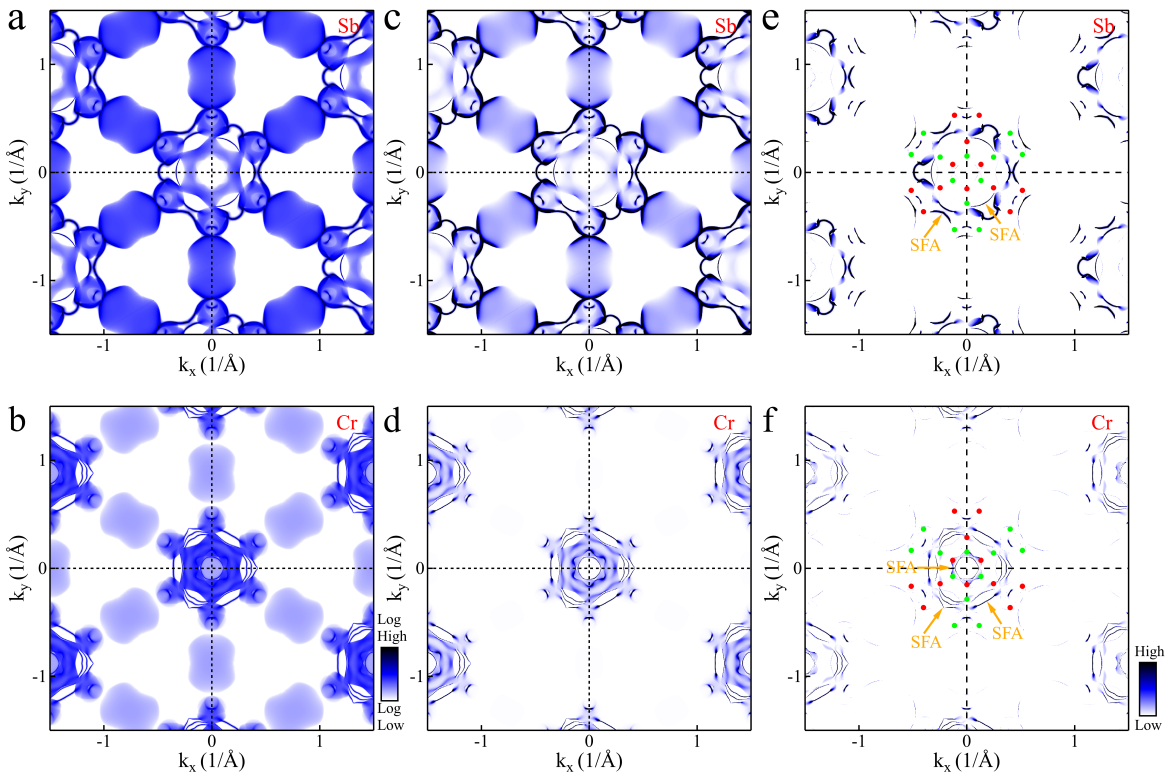

FIG. S5. **Calculated surface spectral densities for CrSb with log and linear color scales.** (a), (c) and (b), (d) are Sb and Cr terminated surfaces,respectively, displayed with log (a-b) and linear (c-d) color scales. (e-f) The DFT calculated surface projected Fermi surface on Sb (e) and Cr (f) terminated surfaces after subtraction of the bulk states. The orange arrows mark the SFAs.

Appendix F: Experimental determination of the surface termination in CrSb

The (0001) surfaces of CrSb can terminate with a triangular-lattice monolayer of either Cr or Sb atoms. Experimentally, we observed two dissimilar Fermi surface structures, as shown in Fig. S6c and S6d. It is natural to assume that these two Fermi surfaces correspond to different surface terminations. To verify this conjecture, we conducted X-ray photoelectron core-level spectroscopy (XPS) measurements (Fig. S6a-S6b) on the two terminations corresponding to the measured Fermi surfaces (Fig. S6c-S6d). The result is that the peak intensity of Cr 3*p* states in Fig. S6a is much lower than that in Fig. S6b, indicating that the XPS measurement in Fig. S6c (Fig. S6d) corresponds to the Sb (Cr) terminated surface.

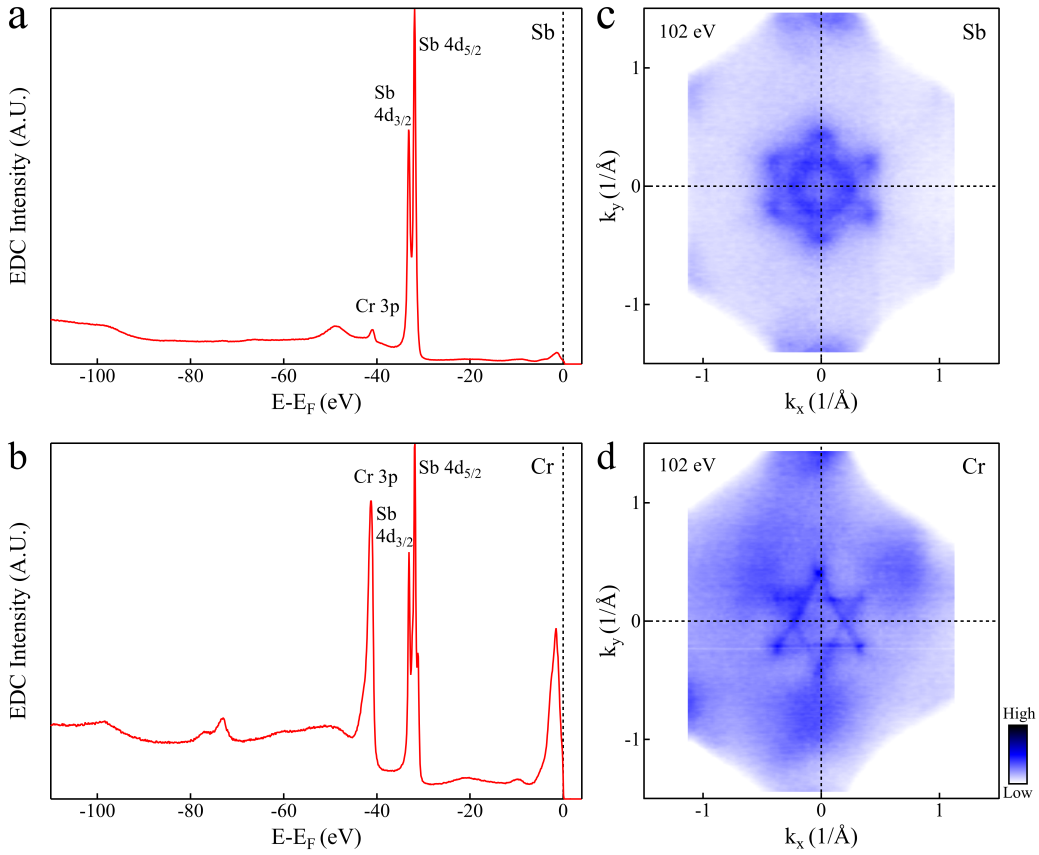

FIG. S6. **Determination of the surface terminations of CrSb.** (a-b) XPS measurements on the (0001) surface measured on Sb (a) and Cr (b) terminated surfaces. The peak intensity of the Cr 3p state for Sb termination is much lower than for Cr termination. (c-d) The Fermi surfaces measured for terminations corresponding to the XPS measurements in (a-b).

After establishing the correspondence between the surface termination and the measured Fermi surfaces, we further compared the latter (Fig. S7b-S7c and Fig. S7e-S7f) with the calculated surface spectral density at the binding energy of 0.25 eV (Fig. S7a-S7b). The calculated spectra of two different terminations are indeed dissimilar, and are both in good agreement with the experiment. For the Sb-terminated surface, the calculated spectral density shows distinct petal-like SFA whose traces are also visible in the curvature of the experimental intensities.

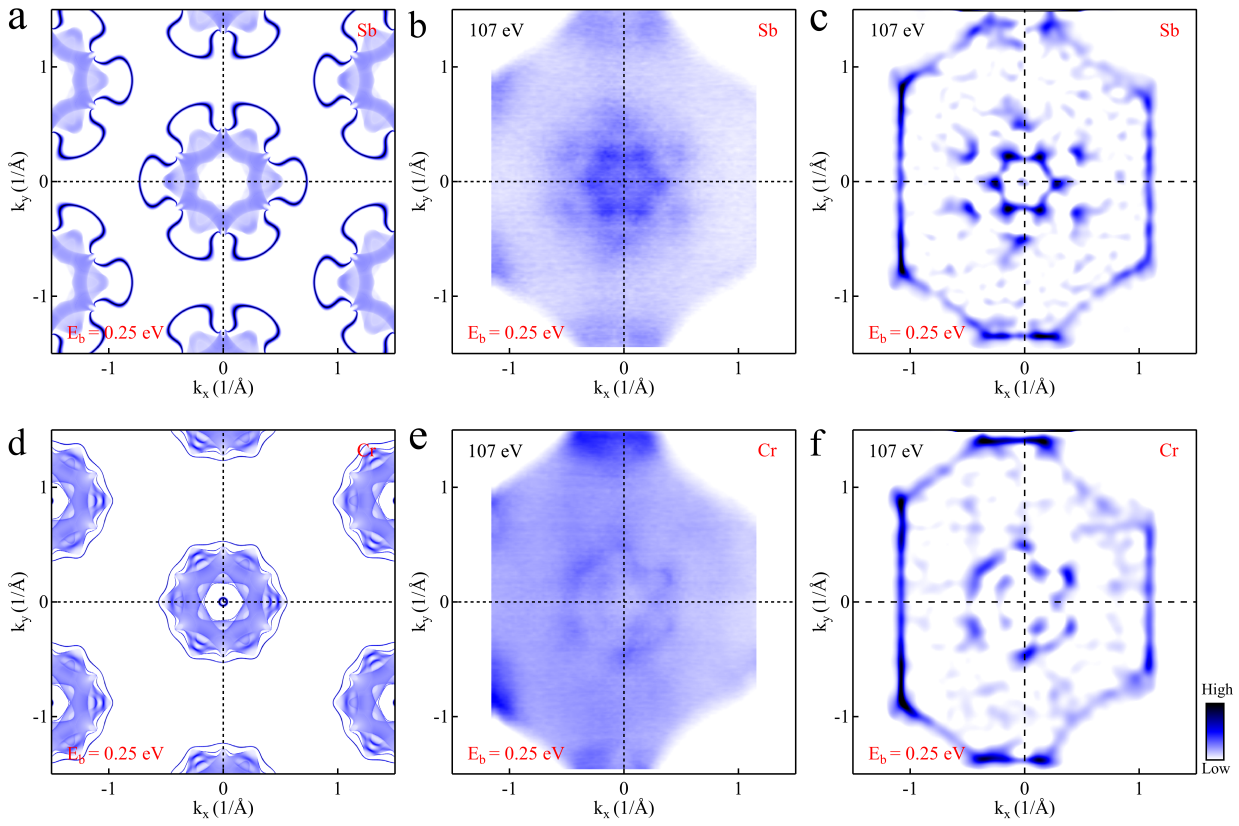

FIG. S7. **Comparison of surface density of states at E_b = 0.25 eV.** (a) and (d): Calculated surface density of states at E_b = 0.25 eV on the Sb terminated and Cr terminated surfaces. (b) and (e) are measured Fermi surfaces at E_b = 0.25 eV on the Sb terminated (b) and Cr terminated (e) surfaces with a photon energy of 107 eV. (c) and (f) are the two dimensional (2D) curvature image of (b) and (e), respectively.

Appendix G: Distinguishing the surface state of the Cr terminated surface

Fig. S8a and S8b show the calculated surface state at the Fermi level of the Cr terminated surface displayed with a log (Fig. S8a) and a linear (Fig. S8b) color scale, respectively. The SFAs of the Cr terminated surface are marked by orange arrows in Fig. S8b. Comparing these measurements, similar features can be observed in the measured constant energy contours, marked by orange arrows in Fig. S8c-S8h, indicating the SFA nature of them.

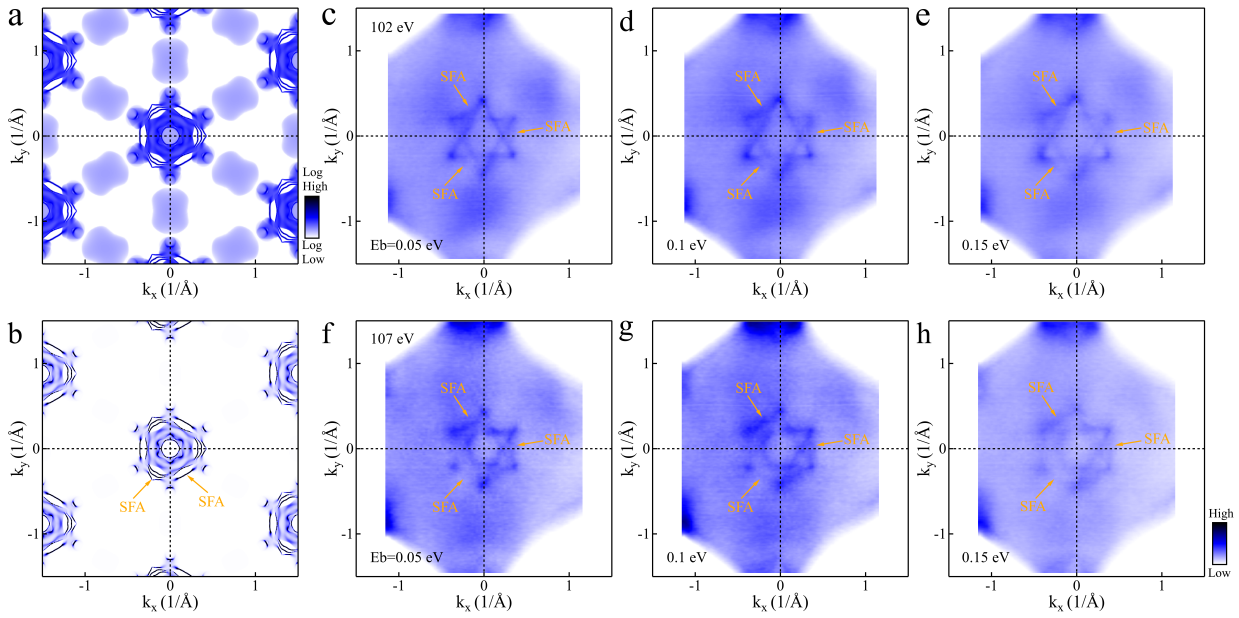

FIG. S8. **Distinguishing the surface states of the Cr terminated surface.** (a-b) Surface projected DFT calculated Fermi surfaces of the Cr terminated surface displayed with log (a) and linear (b) color scale. (c-e) The constant energy contours for the Cr terminated surface measured with a photon energy of 102 eV at the binding energy of 0.05 eV (c), 0.1 eV (d) and 0.15 eV (e). (f-h) The constant energy contours for the Cr terminated surface measured with a photon energy of 107 eV at the binding energy of 0.05 eV (f), 0.1 eV (g) and 0.15 eV (h). The surface states are marked by orange arrows.

Appendix H: Estimation of the energy scale of the maximum band spin splitting in CrSb

According to the DFT bulk band calculations, the maximum band spin splitting is found around the $k_z = 0.4\ \pi/c$ plane. Fig. S9 shows the band dispersion measured with photon energy of 107 eV (see Fig. S9a-S9b) and 112 eV (see Fig. S9c-S9d), corresponding to the k_z planes around $0.4\ \pi/c$. Fig. S9b and S9d are the second derivative images of Fig. S9a and S9c, enhancing the band contrast. The so-estimated band spin splitting amounts to about 0.8 eV for 107 eV (Fig. S9b) and 1 eV for 112 eV (Fig. S9d).

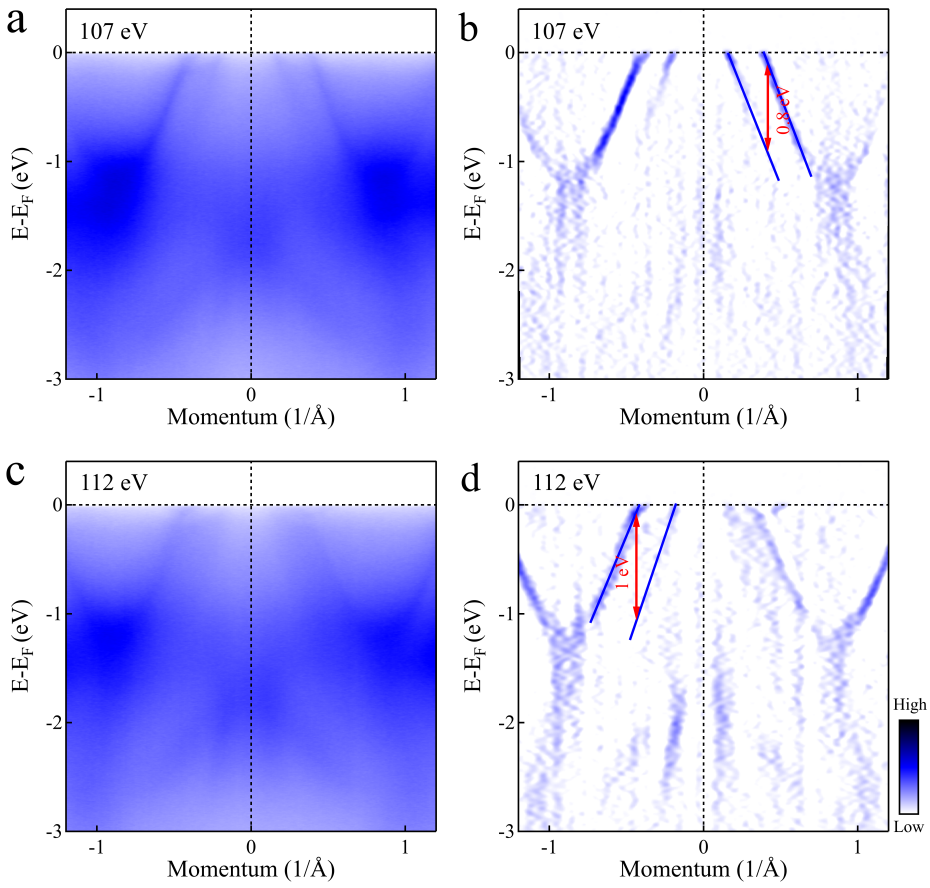

FIG. S9. **Estimating the energy scale of the band spin splitting.** (a) Band dispersion measured with a photon energy of 107 eV along $\overline{\mathrm{M}} - \overline{\Gamma} - \overline{\mathrm{M}}$. (b) The second derivative image of (a). (c-d) Similar measurements as (a-b) but with a photon energy of 112 eV. The measured band spin splitting is 0.8 eV for 107 eV and 1 eV for 112 eV photon energy, respectively.

Appendix I: Observation of two domain structures in CrSb

When performing spatial scans on the Cr terminated surface, we observe that the measured Fermi surface flips at certain positions on the sample surface (Fig. S10a-S10b). This indicates that there are two domain structures on the Cr terminated surface of CrSb.

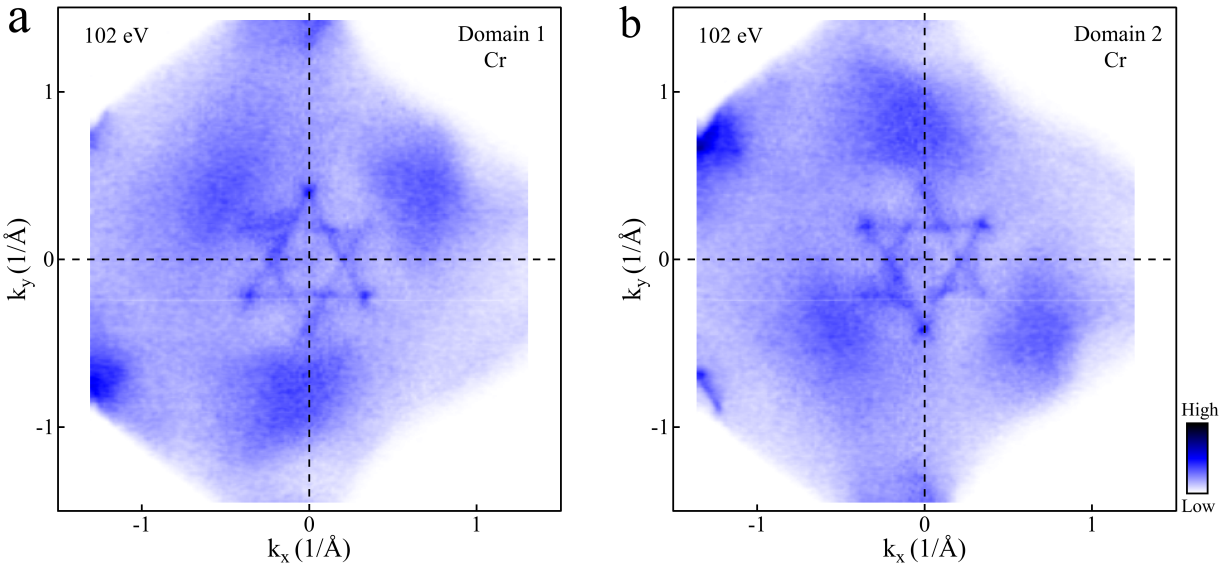

FIG. S10. **Two domain structures on the Cr terminated surface of CrSb.** (a-b) Fermi surface measured with photon energy of 102 eV on domain 1 (a) and domain 2 (b) of the Cr terminated surface.

Appendix J: Photon energy dependent band dispersion measurements

Fig. S11 shows the photon energy dependent band dispersion measurements along the $\overline{\Gamma} - \overline{\mathrm{M}}$ direction on the Cr terminated surface. In order to determine the surface state properties of the band features marked by orange arrows in Fig. S11a-S11e, we analyzed the momentum distribution curves (MDCs). Fig. S11f-S11j show the photon energy dependent MDCs extracted from Fig. S11a-S11e at binding energies of 0.1 eV (Fig. S11f), 0.3 eV (Fig. S11g), 0.5 eV (Fig. S11h), 0.7 eV (Fig. S11i) and 0.9 eV (Fig. S11j). The gray dashed lines in Fig. S11f-S11j mark the MDCs' peak positions, which correspond to the band features marked by orange arrows. The negligible photon energy dependence of the MDC peak positions indicates the surface nature of these band features (marked by orange arrows in Fig. S11a-S11e). By further comparing with the corresponding surface projected bands from the DFT calculations shown in Fig. 4i, we conclude that these features are SFAs.

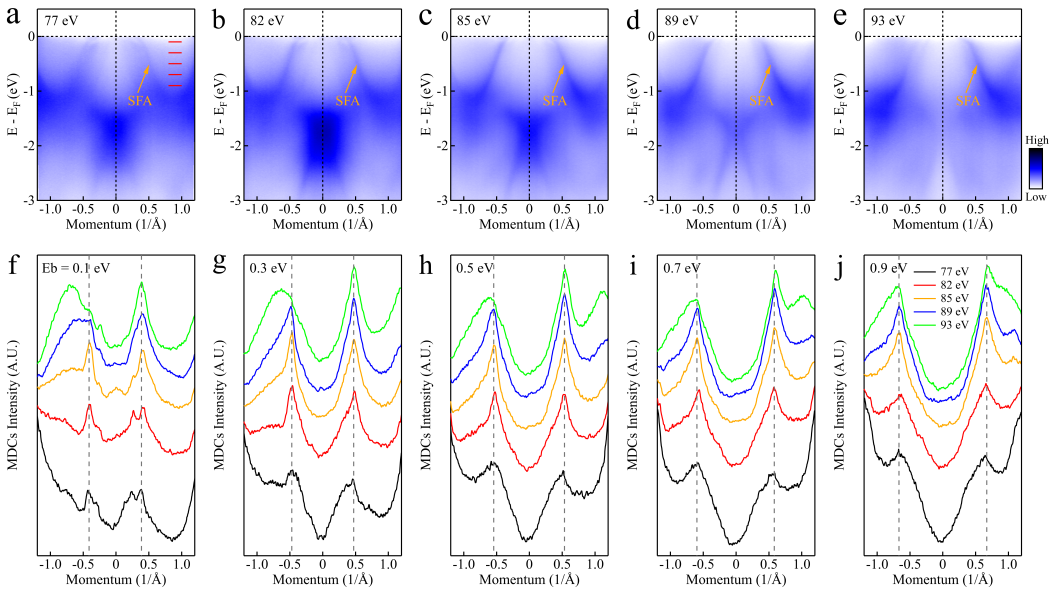

FIG. S11. **Photon energy dependent band dispersion along the $\overline{\Gamma} - \overline{\mathrm{M}}$ direction on the Cr terminated surface.** (a-e) Photon energy dependent band dispersion measurements along $\overline{\Gamma} - \overline{\mathrm{M}}$ on the Cr terminated surface with photon energies of 77 eV (a), 82 eV (b), 85 eV (c), 89 eV (d) and 93 eV (e). (f-j) The photon energy dependent MDCs extracted from (a-e) at the binding energies of 0.1 eV (f), 0.3 eV (g), 0.5 eV (h), 0.7 eV (i) and 0.9 eV (j). The MDC peak positions are marked by dashed vertical lines in (f-j). Energies of the MDCs are marked in (a) by red lines.

Fig. S12 shows the photon energy dependent band dispersion measurements along the $\overline{\Gamma}-\overline{\mathrm{K}}$ direction on Sb (Fig. S12a-S12e) and Cr (Fig. S12f-S12j) terminated surfaces. Fig. S12k and S12l show the extracted MDCs from Fig. S12a-S12e and Fig. S12f-S12j at a binding energy of 0.2 eV. The gray dashed lines in Fig. S12k and S12l mark the MDC peaks corresponding to the bands marked by orange arrows in Fig. S12a-S12e and Fig. S12f-S12j. Also in this case, the negligible photon energy dependence of the MDC peaks (Fig. S12k and S12l) indicate the surface nature of the bands marked by orange arrows in Fig. S12a-S12e and Fig. S12f-S12j. Comparing with the corresponding DFT calculated surface states shown in Fig. 4p and 4s, the SFA nature of the states can be determined.

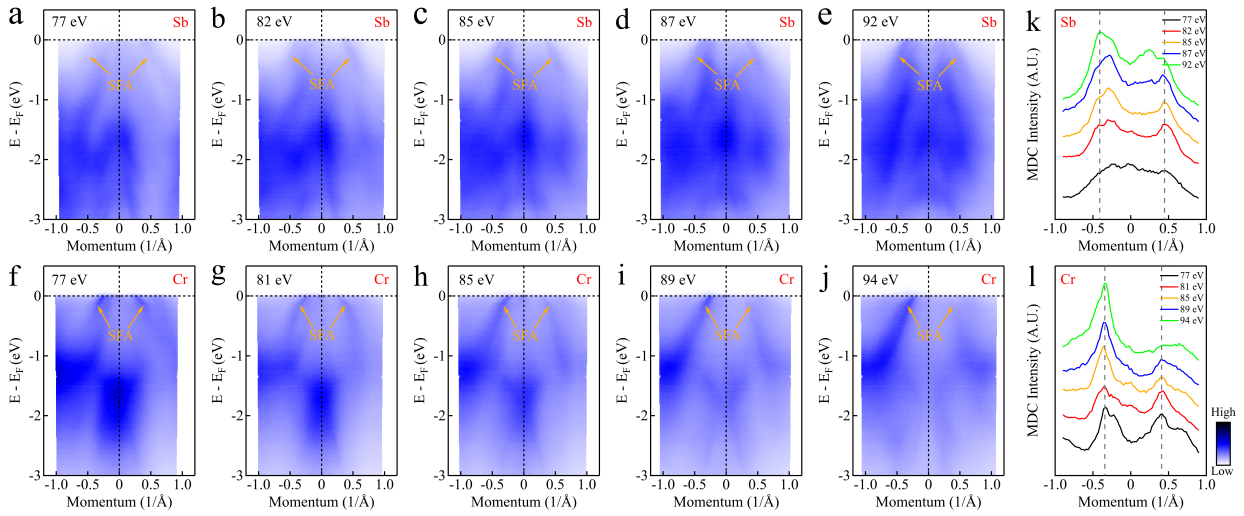

FIG. S12. **Photon energy dependent band dispersion along $\overline{\Gamma}-\overline{\mathrm{K}}$ on Sb and Cr terminated surfaces.** (a-e) The photon energy dependent band dispersion measurements along the $\overline{\Gamma}-\overline{\mathrm{K}}$ direction on the Sb terminated surface with photon energies of 77 ev (a), 82 eV (b), 85 eV (c), 87 eV (d) and 92 eV (e). (f-j) The photon energy dependent band dispersion measurements along the $\overline{\Gamma}-\overline{\mathrm{K}}$ direction on the Cr terminated surface with photon energies of 77 ev (f), 81 eV (g), 85 eV (h), 89 eV (i) and 94 eV (j). (k-l) The MDCs extracted from (a-e) and (f-j) at a binding energy of 0.2 eV. The MDC peaks marked by gray dashed lines in (k) and (l).

Appendix K: Nodal line and drumhead surface state in CrSb without SOC

The topological nodal line appears in systems with a band crossing and forms a closed loop. It is often constrained to a high symmetry line or plane, protected by inversion, mirror, and spin rotation symmetry [5–8]. In the absence of SOC, time-reversal symmetry (T), with the symmetry operator $T = \mathcal{K}$ (complex conjugation) for one spin sector, is automatically preserved, and inversion symmetry is present in the space group. The combination of time-reversal symmetry and inversion symmetry (PT) is thus preserved across the entire BZ. In the following, we present the PT symmetry protected nodal line and its corresponding drumhead surface state.

Around the Fermi level, we found three sets of nodal lines (see Fig. S13a and Fig. S14a-S14c). To reveal their topological properties, we employ a Berry phase calculation along those nodal lines. As shown in Fig. S13a and Fig. S14c, all nodal lines have an integrated Berry phase $\pm\pi$ at the red circle, reflecting their nontrivial topology. Since the density of states above the Fermi level is relatively large, we only focus on occupation band number 8 and 9 in the following discussion. We then calculate the Wannier charge center (WCC) along the high symmetry lines labelled in Fig. S13c and the surface state calculation to determine the drumhead surface state on the (001) surface. As shown in Fig. S13b-S13d, the change of the WCC is always associated with a crossing of the nodal line (labelled as filled and open points for occupation band number 8 and 9, respectively). The energies of these crossing points in Fig. S13b from left to right are: -0.34722, -1.51709, -1.55667, -1.27092, -6.80210 for band 8, and -0.10452, -0.00590 for band 9. As a double check, we show the three corresponding drumhead surface states in Fig. S13d, all of which possess starting/ending points aligned with the WCC jump positions in Fig. S13b. We note that, due to the coincidence of the projected nodal line and $\overline{\Gamma} - \overline{M}$ path, we choose a path that slightly deviated from $\Gamma - M$ in the WCC simulations. Despite this, the WCC result in Fig. S13b matches well with the drumhead surface states in Fig. S13d.

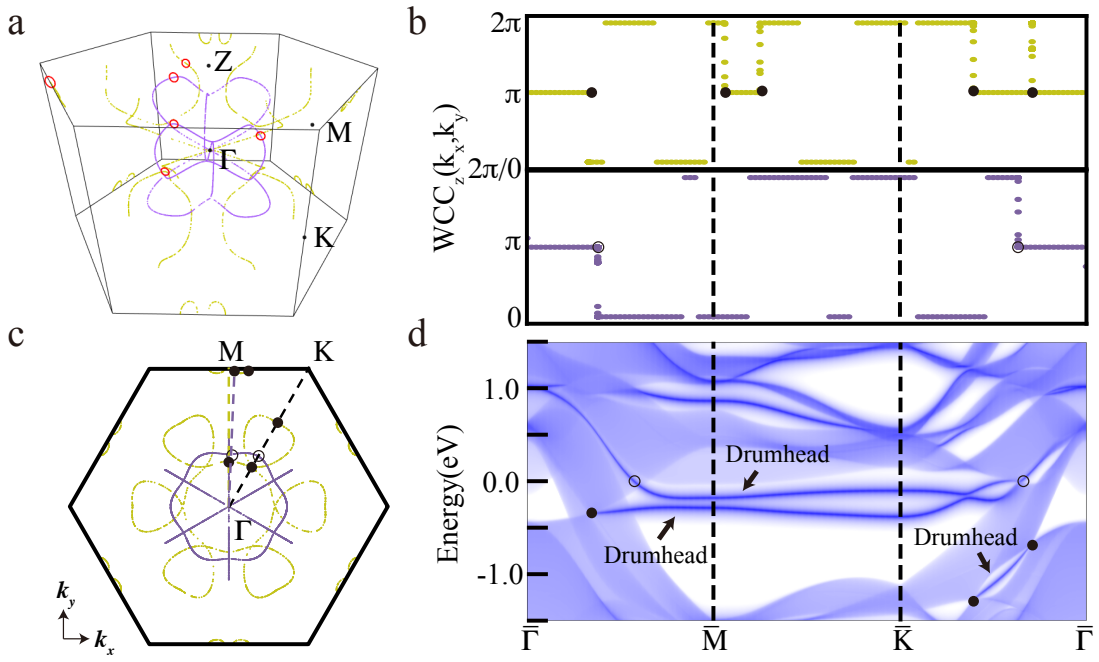

FIG. S13. **nodal line and surface states in the spin-up channel** (a) nodal line distribution in the 1^{st} BZ where the yellow and purple dots represent the nodal lineswith occupation number 8 and 9, respectively. (b) Wannier charge center (WCC) results along the high symmetry lines $\Gamma - M - K - \Gamma$ and integrated along: k_z. Upper and lower panel represent the occupation number 8 and 9, respectively. (c) The top view of nodal line distribution with high symmetry lines. Open and filled circles indicate positions where the WCC jump happens in (b). (d) Surface state results on the (001) Sb terminated surface. The drumhead surface state and the corresponding projected nodal line position is labelled.

Appendix L: SOC induced nodal line to same-spin WPs

As discussed in the last section, the nodal line exists in CrSb for both the spin-up and spin-down channel without SOC. In Fig. S14a-S14c, the corresponding same-spin WPs are denoted in their SOC-free nodal lines. From Fig. S14a to S14c, they are the same-spin WPs No. 3.2 and nodal line between band 8 and 9, No. 3.3 nodal line between band 9 and 10, and No. 3.1 nodal line between band 9 and 10. This SOC-induced topological nodal line to Weyl semimetal transition [5] has also been reported in TaAs[9, 10] and ZrTe[11]. Here, we found two same-spin WP groups along the projected high symmetry line: $\overline{\Gamma} - \overline{M}$ that are

also discussed in the main-text. These two sets of WPs also give rise to long surface states across the surface BZ. WPs No. 3.1 are buried in the bulk state and in Fig. S14e, clear surface state signal is shown in the pure surface state calculation results. Due to the large density of states above the Fermi level, many more WPs may be found in the conduction band region. Based on the spin-polarized Fermi arcs, the evidence of a nodal line to WPs transition, and the altermagnetic nature of CrSb with weak SOC, we conclude that the surface states in the vicinity of the Fermi level are topological.

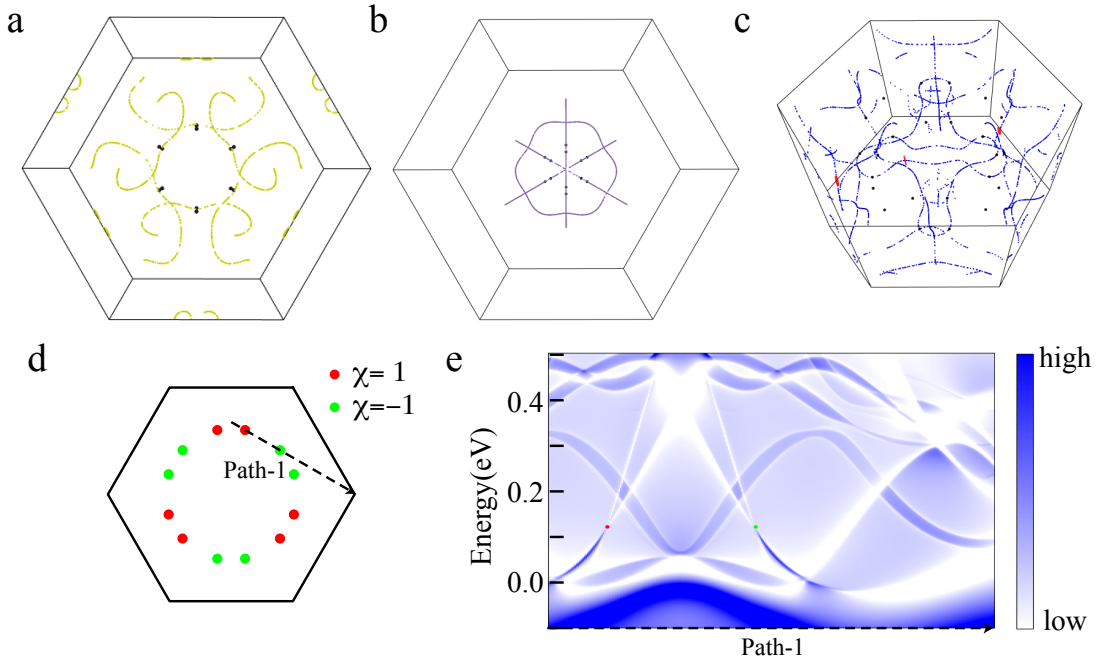

FIG. S14. **nodal line and same-spin WPs** (a)-(c) are the same-spin WPs distribution and the corresponding nodal linesbetween N and $N+1$. The nodal linesare calculated in the spin-up channel without SOC and the WPs are the three same-spin WPs groups in Sec. 2. (c) WPs distribution of No. 3.1 with chirality denoted. The surface state on the (001) Sb terminated surface along the Path-1 denoted in (d) is presented in (e). (e) The pure surface state spectral density with the bulk state density subtracted.

Appendix M: Spin-polarized surface state and corresponding same-spin WPs

As the same-spin WPs can host different topological charges, the corresponding Fermi arc on the surface is naturally spin-polarized. The upper panel in Fig. S15 shows the surface state from same-spin WPs No. 3.2, while the lower panel shows the surface state originating from the energy $E \approx E_f + 0.3$ eV and belongs to WPs No. 3.3. On the (001) surface, two WPs with the same chirality are projected onto the same location once they are out of the $k_z = 0$ plane. The total chirality $\chi = \pm 2$ of WPs No. 3.2 then results in two surface states, as shown in Fig. S3c-S3d. One of these surface states disperses towards the Γ point and another backwards. In Fig. S15 upper panel, the Fermi arc at $E = E_f - 0.25$ eV only includes one of the branches from the surface state of WPs No. 3.2. The petal-like surface states are from the drumhead surface state without SOC and half of them are now protected by the WPs with SOC. This explains the Fermi arcs in the upper panel of Fig. S15: the nodal line to WPs transition is driven by SOC and preserves the Fermi arcs. Since all the WPs contributing to the long Fermi arcs are of the same-spin type and their Fermi arcs dispersions are surface dependent, their corresponding Fermi arcs are spin-polarized and also separated on different terminations.

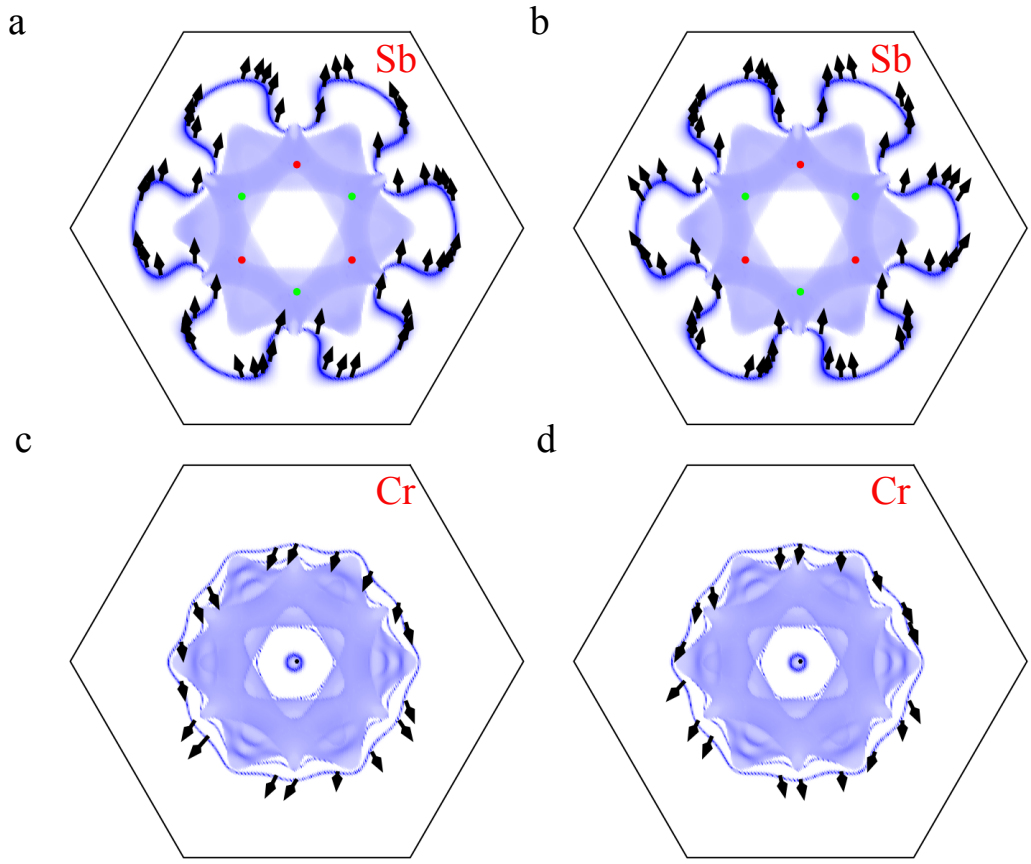

FIG. S15. **Surface states at $E = E_f - 0.25$ eV with spin texture** (a) and (b) are surface states on the Sb terminated surface with the WPs No. 3.2 denoted; (c) and (d) are surface states on the Cr terminated surface. The corresponding spin textures are indicated by arrows where the $s_x - s_z$ and $s_y - s_z$ projections are shown in the left and right panel, respectively.

[1] D. Gresch *et al.*, Automated construction of symmetrized Wannier-like tight-binding models from ab initio calculations. Phys. Rev. Materials **2**, 103805 (2018).

[2] Y. X. Zhao and A. P. Schnyder, Nonsymmorphic symmetry-required band crossings in topological semimetals. Phys. Rev. B **94**, 195109 (2016).

[3] L. Muechler *et al.*, Topological nonsymmorphic metals from band inversion. Phys. Rev. X **6**, 041069 (2016).

[4] M. Hu *et al.*, Realistic tight-binding model for monolayer transition metal dichalcogenides of 1T' structure. Phys. Rev. B **104**, 035156 (2021).

[5] C. Fang *et al.*, Topological Nodal Line Semimetals. Chin. Phys. B **25**, 117106 (2016).

[6] I. Robredo, *et al.*, Theoretical study of topological properties of ferromagnetic pyrite CoS_2. J. Phys. D: Appl. Phys. **55**, 304004 (2022).

[7] N. B. M. Schröter, *et al.*, Weyl fermions, Fermi arcs, and minority-spin carriers in ferromagnetic CoS_2. Sci. Adv., 2020, **6**: eabd5000.

[8] Y.M. Xie *et al.*, Kramers nodal line metals. Nat. Commun. **12**, 3064 (2021).

[9] H. Weng, *et al.*, Weyl Semimetal Phase in Noncentrosymmetric Transition-Metal Monophosphides. Phys. Rev. X **5**, 011029 (2015).

[10] S. Huang, *et al.*, A Weyl Fermion semimetal with surface Fermi arcs in the transition metal monopnictide TaAs class. Nat. Commun. **6**, 7373 (2015).

[11] H. Weng, *et al.*, Coexistence of Weyl fermion and massless triply degenerate nodal points. Phys. Rev. B **94**, 165201 (2016).